Cite as: F. Rao *et al.*, *Science* 10.1126/science.aao3212 (2017).

Reducing the stochasticity of crystal nucleation to enable subnanosecond memory writing

Feng Rao,[1,2*†] Keyuan Ding,[1,2*] Yuxing Zhou,[3*] Yonghui Zheng,[1] Mengjiao Xia,[4] Shilong Lv,[1] Zhitang Song,[1†] Songlin Feng,[1] Ider Ronneberger,[5] Riccardo Mazzarello,[5] Wei Zhang,[3†] Evan Ma[3,6]

[1]State Key Laboratory of Functional Materials for Informatics, Shanghai Institute of Micro-system and Information Technology, Chinese Academy of Sciences, Shanghai 200050, China. [2]College of Materials Science and Engineering, Shenzhen University, Shenzhen 518060, China. [3]Center for Advancing Materials Performance from the Nanoscale, State Key Laboratory for Mechanical Behavior of Materials, Xi'an Jiaotong University, Xi'an 710049, China. [4]International Laboratory of Quantum Functional Materials of Henan, School of Physics and Engineering, Zhengzhou University, Zhengzhou 450001, China. [5]Institute for Theoretical Solid State Physics, JARA-FIT and JARA-HPC, RWTH Aachen University, Aachen D-52074, Germany. [6]Department of Materials Science and Engineering, Johns Hopkins University, Baltimore, MD 21218, USA.

*These authors contributed equally to this work.

[†]Corresponding author. Email: fengrao@mail.sim.ac.cn (F.R.); ztsong@mail.sim.ac.cn (Z.S.); wzhang0@mail.xjtu.edu.cn (W.Z.)

Operation speed is a key challenge in phase-change random-access memory (PCRAM) technology, especially for achieving subnanosecond high-speed cache-memory. Commercialized PCRAM products are limited by the tens of nanoseconds writing speed, originating from the stochastic crystal nucleation during the crystallization of amorphous $Ge_2Sb_2Te_5$. Here, we demonstrate an alloying strategy to speed up the crystallization kinetics. The $Sc_{0.2}Sb_2Te_3$ compound we designed allows a writing speed of only 700 picoseconds without preprogramming in a large conventional PCRAM device. This ultrafast crystallization stems from the reduced stochasticity of nucleation through geometrically matched and robust ScTe chemical bonds that stabilize crystal precursors in the amorphous state. Controlling nucleation through alloy design paves the way for the development of cache-type PCRAM technology to boost the working efficiency of computing systems.

Nonvolatile phase-change random-access memory (PCRAM) is regarded as a leading candidate for next-generation electronic memory hierarchy (*1*–*6*). It utilizes the pronounced electrical resistance difference between the amorphous and crystalline states of chalcogenide phase change materials (PCMs) to encode digital information (*4*). Large fragility, i.e., strong deviation of the temperature dependence of atomic dynamics from Arrhenius behavior (*7*), is an essential property of PCMs that guarantees fast and reversible phase transitions between the two states at elevated temperatures, and yet good thermal stability at room temperature, making PCRAM one of the most promising candidates to compete with dynamic random access memory (DRAM) and Flash memory (*8*–*10*). However, to achieve "universal memory" (*1*) with PCRAM, subnanosecond operation is needed to compete with cache-type static random-access memory (SRAM) (*5*). Proper thermal design of PCRAM devices allows for an ultrafast RESET process through amorphization, while the SET process remains as the bottleneck, because the crystallization kinetics of PCMs is critically limited by their fundamental properties, such as nucleation rate and growth speed. Several strategies have been tried to improve the SET or writing speed of the current $Ge_2Sb_2Te_5$ (GST)-based PCRAM devices by increasing the crystallization speed of GST, but the typical writing time is still of tens of ns. A very fast SET speed of ~500 ps (*11*) was achieved on a ~30 nm pore-like GST-based PCRAM device with the aid of a constant low voltage. However, because a ~10 ns long preprogramming treatment was needed prior to every SET operation, the real overall writing speed remains insufficient for sub-ns cache-type memory applications.

The abundance of four-fold ABAB rings (A = Ge/Sb, B = Te) in the amorphous state (*12*, *13*) has been proposed to be the mechanism for fast crystallization in GST, as the ABAB rings are the smallest structural units in the recrystallized cubic rocksalt phase, and two such structural motifs can form a cube. We call this structural order a crystalline precursor, as it shares the same feature of the corresponding crystalline structure. Crystalline precursors are related to subcritical embryos, but do not necessarily imply the presence of quenched-in crystal nuclei. Upon heating to elevated temperatures (e.g., 600 K), atoms in the amorphous state become highly mobile, and rings and cubes fluctuate in and out constantly. A tremendous number of atomic configurations over a long incubation period need to be sampled before the critical nucleus is obtained (*14*–*16*) due to high frequency of formation and dissolution of crystalline precursors. Even in ab initio molecular dynamics simulations, the crystallization time at 600 K of models containing several hundreds of atoms can fluctuate considerably, varying from several hundreds of picoseconds to many nanoseconds, reflecting the stochastic nature of the incubation process (*16*–*19*). To alleviate this, (*11*) introduced a long (~10 ns) pretreatment to preseed nuclei inside the amorphous matrix, such that the ensuing SET operation becomes primarily crystal growth. Instead, our goal is to achieve ultrafast crystallization by

altering the intrinsic nucleation properties of the phase-change material itself to enable real sub-ns memory writing.

Our design principle was to find materials with enhanced thermodynamic driving force to stabilize crystalline precursors, in this case robust ABAB rings and cubes, to drastically extend their lifetime during the incubation period. We also desire as much as possible geometric conformability between the crystalline precursor in the amorphous phase and the corresponding crystalline counterpart, to reduce the interface energy. These two traits together, i.e., the dynamical stability and structural similarity, are projected to dramatically decrease the energy barrier for crystal nucleation (*20*, *21*). In order to accomplish this goal, we introduced an alloying element to promote geometrically-matched and high-strength chemical bonds to stabilize the crystal precursors. The most widely used PCMs are GeSbTe compounds along the pseudo-binary line between GeTe and Sb_2Te_3 (*22*, *23*). Here, we used Sb_2Te_3 as the parent phase to avoid the additional complexity of tetrahedral motifs found in amorphous GeTe and GeSbTe that arise from homopolar Ge-Ge bonds formed during fast quenching (*24–26*), because such motifs may hinder the crystallization into the octahedrally coordinated rocksalt phase. Antimony telluride is a prototype topological insulator with ordered quintuple layers connected via van der Waals forces, and it can also be made in a metastable rocksalt state (Fig. 1A) for phase change application (*27*). Alloying elements such as transition metals into antimony telluride, e.g., $Ti_{0.4}Sb_2Te_3$ (TST), can lead to superior crystallization speed as compared to GST (*28*), but the segregated triple-layered $TiTe_2$ nano-lamellae (*29*) prevent further reduction of crystallization time into sub-ns scale, stemming from the fact that none of the crystalline titanium tellurides match with the cubic rocksalt lattice structure of Sb_2Te_3.

Therefore, we performed a systematic materials screening of other transition metal tellurides (TMTs). We used two essential criteria to select the transition metal alloying element that best promotes high-fidelity crystalline precursors. The crystal-like structural motifs in the amorphous state should be (i) geometrically-matched as much as possible to the rocksalt crystalline product Sb_2Te_3, and (ii) further stabilized by the added transition metal alloying element if its incorporation brings in chemical bonds of high strength. The first criterion requires a local cubic geometry with coordination number of 6 and bond lengths close to 3.0 Å (Fig. 1A). For the second criterion, we regarded the melting temperature (T_m) and cohesive energy (E_{coh}) as the key indicators. From all the TMTs with T_m > 900 K listed in Fig. 1A, we identify only six suitable candidates, i.e., TM = Sc, Mn, Zn, Y, Cd, and Hg, that satisfied the geometric conformability criterion (fig. S1). Cubic rocksalt scandium telluride Sc_2Te_3 is of particular interest, as it also has a high content of intrinsic atomic vacancies (1/3) on the cation-like sublattice, same as rocksalt Sb_2Te_3 (Fig. 1B and fig. S1). We calculated the E_{coh} for the six rocksalt TMTs with density functional theory (DFT) simulations (*30*). The more negative value of E_{coh} corresponds to stronger TM-Te bonds (Fig. 1A). This ruled out MnTe and HgTe, as their E_{coh} is unfavorable with respect to that of base-alloy rocksalt Sb_2Te_3 (-0.06 eV/atom). For the other four transition metals, DFT simulations on the rocksalt TM-Sb_2Te_3 revealed that Zn or Cd atoms resulted in too severe lattice distortions in the crystalline phase. Yttrium is not ideal because the local motifs around Y atoms in the amorphous state can no longer keep the (defective-) octahedral coordination, which may hinder the crystallization kinetics (fig. S2).

Scandium is therefore singled out as the most appealing alloying element according to the above criteria. We further cross-checked the chemical stability of Sc_2Te_3 by employing a more sophisticated method before synthesizing Sc-incorporated Sb_2Te_3 alloys. We performed crystal orbital Hamilton populations (COHP) analysis, which dissects electronic density of states (DOS) into bonding (stabilizing) and antibonding (destabilizing) interactions (*30*). The antibonding contribution of both rocksalt Sb_2Te_3 and Sc_2Te_3 at the Fermi level E_F is marginal (Fig. 1B), indicating good stability of both systems. In Sb_2Te_3, we found an antibonding region right below E_F. In contrast, Sc_2Te_3 had all the filled bands up to the E_F making stabilizing contributions, suggesting that Sc_2Te_3 is more robust as compared to Sb_2Te_3. In this comparison both compounds are in exactly the same geometrical configuration (Fig. 1B), including the random distribution of atomic vacancies and lattice parameter, for the DFT simulations and COHP analyses (fig. S3).

Then we alloyed small concentration of scandium into antimony telluride via magnetron sputtering (*30*). In general, too little scandium leads to poor thermal stability of the amorphous phase, while too much scandium makes our device fabrication difficult. Balancing the two led to the composition of $Sc_{0.2}Sb_2Te_3$ (SST) for thorough experiments. The SST thin film we obtained was amorphous with a crystallization temperature of ~170°C (Fig. 2A), similar to that of GST. We conducted electrical transport experiments on both SST and GST films upon heating, which gave similar sheet resistance profiles, as well as three resistance windows, same as the GST, corresponding to three solid phases of SST, namely amorphous, cubic and hexagonal (*31*). We performed transmission electron microscopy (TEM) experiments to access the detailed structural properties of the SST film. The bright-field (BF) image (Fig. 2B) and the corresponding selected area electron diffraction (SAED) pattern (Fig. 2C) of the SST film annealed at 270°C show a homogeneously polycrystalline morphology with numerous nano-sized crystal grains, suggesting that SST is a nucleation-dominant material. The SAED pattern was indexed as rocksalt type, following the selection rules for crystal structures (*32*). The rocksalt structure was further confirmed with high-resolution TEM images (Fig. 2, D to F) of three (coexisting) specific crystal grains (boxed in Fig. 2B). In situ heating TEM experiments reveal the successive structural transformations from amorphous to

rocksalt and then to hexagonal phase in the SST film (fig. S4). Because the temperature window of rocksalt SST is comparable to that of GST, reversible and rapid phase transitions between the amorphous and rocksalt states are expected in SST-based PCRAM device through the design of a suitable heating profile. Just like GST, the equilibrium hexagonal phase needs to be avoided in the SET process because the transition to this phase is a relatively slow process, and the melting of the rigid hexagonal phase entails a high energy cost (*27*).

We fabricated SST based T-shaped PCRAM devices by using 0.13 μm node complementary metal-oxide semiconductor technology (inset of Fig. 3A) (*30*). GST, Sb_2Te_3 and TST devices of the same size were also made to enable a direct comparison. We altered the voltage pulses from ns to ps width with the magnitude ranging from ~1.0 V to ~5.5 V, and applied them to the devices (fig. S5). As the magnitude of voltage pulse increases, the SET speed of all the devices becomes faster (Fig. 3A and fig. S6), with SST being one order of magnitude faster than GST at all voltages. The fastest SET process for the GST device needs ~10 ns to complete, while that of the SST device requires only ~700 ps. This SET speed is at the limit of PCRAM, as no preprogramming is needed for SST, and is already comparable to the resistance switching speed based on the so called threshold switching effects (*33*). For the latter the low-resistance state disappeared instantly with electric field removal (*33*), whereas the transition in our SST is permanent, and the low-resistance crystalline state is very stable. The SST device showed a cyclability of ~10^5 under the sub-ns switching conditions (Fig. 3B). Up to ~4×10^7 cyclability was achieved by reducing the voltage bias while increasing the pulse width to tens of ns (fig. S7).

The sub-ns crystallization speed of SST originates from the presence of the ~4% Sc added into the Sb_2Te_3 base alloy, as the fastest SET speed of the Sb_2Te_3 device is ~6 ns. For Sb_2Te_3 the absence of complexity through the introduction of Ge already improves the crystallization kinetics as compared to GST, but is still insufficient to drive the SET speed down to sub-ns level (fig. S6). We performed density functional theory based molecular dynamics (DFMD) simulations at finite temperatures (*30*) to elucidate the crystallization mechanism in SST, and in particular the role of Sc. We studied the structural properties of the amorphous models, which we generated using the melt-quench scheme (*12*, *25*). Four-fold rings are the dominant structural motif in amorphous SST (Fig. 4A), just like GST. More importantly, we found that every Sc atom was involved in at least one four-fold ABAB ring (A = Sc/Sb, B = Te), whereas ~80-90% of Sb atoms formed ABAB rings. This structural feature provides an essential ingredient for the high nucleation rate in SST. If the structural motif in the amorphous phase differs considerably from the crystalline phase, such as in the growth-driven PCM $Ag_4In_3Sb_{67}Te_{26}$ (AIST), where five-fold rings dominate, the nucleation rate is very low (*34*, *35*). This structural dissimilarity originates from both the parent compound Sb_2Te and the alloying Ag/In (*35*, *36*).

We found at elevated temperature ~600 K, GST and SST show distinctly different behaviors: Ge(Sb)-Te-Ge(Sb)-Te rings break and reform frequently and rapidly with a very short lifetime on the order of ~5 ps (fig. S8); in stark contrast, the robust Sc-Te-Sc-Te rings stay intact for over 50 ps (Fig. 4, B and C). The long lifetime of ScTe rings stems from the stronger ScTe bonds, and once two such rings get close to form a cube, the latter does not break easily (Fig. 4B and fig. S9). This behavior is obviously different from that of GST, where a sizeable crystalline cluster made of many connected cubes needs to form to prevent fast dissolution (*14*), and even an embedded crystalline seed containing as many as 58 atoms (in a 460 atom GST model) disappears rapidly at ~600 K (*16*). Such an embedded seed had to be fully fixed, to enable quick crystallization through crystal growth in GST (*37*). In contrast, a crystalline precursor made of ScTe cubes (~50 atoms in a 4×4×4 SST supercell made of 428 atoms) can stand robust against thermal fluctuations at ~600 K in the absence of artificial constraint, serving as the center for subsequent crystallization (Fig. 4D). In normal crystallization, a wide distribution of subcritical nuclei of varying sizes develops, and these embryos fluctuate in and out, with only a minute fraction of them evolving into critical nuclei (*34*, *38*). In SST, the long lifetime of crystalline precursors due to the strong ScTe bonds allows for a quicker build-up of precursors on the verge of becoming nuclei or even quenched-in nuclei during phase change operations, which leads to a superior SET speed in PCRAM devices. The particular ScTe seed we introduced in our simulations is not necessarily already a nucleus above the critical size, because the latter is difficult to determine quantitatively from DFMD simulations due to reasonable statistical sampling being computationally too expensive. Nevertheless, the size of the critical nucleus of SST should be smaller than that of GST, as the two compounds share the same interatomic distance, similar diffusion properties (the bulk diffusivity of both SST and GST is of the order of 1×10^{-10} m^2/s at ~600 K), and yet SST crystallizes so much faster in our simulations (*38*).

To utilize SST for practical use, data retention at room temperature, RESET speed and power consumption are also important aspects. As stated before, ~4 at% of scandium added to antimony telluride already improved the thermal stability of the amorphous SST to compete with GST (Fig. 2A). The data retention of the RESET state in SST device is estimated to be ~87°C for 10 years, very similar to that of GST (~82°C for 10 years) (fig. S10). This stability is due to suffocated diffusion in SST at low temperatures. However, scandium addition should not be excessive so as not to make the growth kinetics too sluggish at elevated temperatures for the desired crystallization. Regarding the RESET speed and energy, sub-ns RESET operation was achieved in SST device (fig. S6), and the RESET energy was one order of magnitude lower than GST device due to the easier melting of rocksalt SST (fig.

S11). We believe several strategies, such as scaling down the device size and fine-tuning the material composition, can improve the device performance further (*39*, *40*) to rival SRAM, thus opening up the possibility to develop a truly universal memory. Our work is an example demonstrating the benefit of approaching the problem from materials design, taking advantage of known physical metallurgy principles to control nucleation and growth.

REFERENCES AND NOTES

1. M. Wuttig, Phase-change materials: Towards a universal memory? *Nat. Mater.* **4**, 265–266 (2005). doi:10.1038/nmat1359 Medline
2. F. Xiong, A. D. Liao, D. Estrada, E. Pop, Low-power switching of phase-change materials with carbon nanotube electrodes. *Science* **332**, 568–570 (2011). doi:10.1126/science.1201938 Medline
3. S. W. Nam, H. S. Chung, Y. C. Lo, L. Qi, J. Li, Y. Lu, A. T. Johnson, Y. Jung, P. Nukala, R. Agarwal, Electrical wind force-driven and dislocation-templated amorphization in phase-change nanowires. *Science* **336**, 1561–1566 (2012). doi:10.1126/science.1220119 Medline
4. M. H. Lankhorst, B. W. Ketelaars, R. A. Wolters, Low-cost and nanoscale non-volatile memory concept for future silicon chips. *Nat. Mater.* **4**, 347–352 (2005). doi:10.1038/nmat1350 Medline
5. H. S. Wong, S. Salahuddin, Memory leads the way to better computing. *Nat. Nanotechnol.* **10**, 191–194 (2015). doi:10.1038/nnano.2015.29 Medline
6. R. E. Simpson, P. Fons, A. V. Kolobov, T. Fukaya, M. Krbal, T. Yagi, J. Tominaga, Interfacial phase-change memory. *Nat. Nanotechnol.* **6**, 501–505 (2011). doi:10.1038/nnano.2011.96 Medline
7. C. A. Angell, Formation of glasses from liquids and biopolymers. *Science* **267**, 1924–1935 (1995). doi:10.1126/science.267.5206.1924 Medline
8. J. Orava, A. L. Greer, B. Gholipour, D. W. Hewak, C. E. Smith, Characterization of supercooled liquid $Ge_2Sb_2Te_5$ and its crystallization by ultrafast-heating calorimetry. *Nat. Mater.* **11**, 279–283 (2012). doi:10.1038/nmat3275 Medline
9. R. Jeyasingh, S. W. Fong, J. Lee, Z. Li, K. W. Chang, D. Mantegazza, M. Asheghi, K. E. Goodson, H. S. Wong, Ultrafast characterization of phase-change material crystallization properties in the melt-quenched amorphous phase. *Nano Lett.* **14**, 3419–3426 (2014). doi:10.1021/nl500940z Medline
10. A. Sebastian, M. Le Gallo, D. Krebs, Crystal growth within a phase change memory cell. *Nat. Commun.* **5**, 4314 (2014). doi:10.1038/ncomms5314 Medline
11. D. Loke, T. H. Lee, W. J. Wang, L. P. Shi, R. Zhao, Y. C. Yeo, T. C. Chong, S. R. Elliott, Breaking the speed limits of phase-change memory. *Science* **336**, 1566–1569 (2012). doi:10.1126/science.1221561 Medline
12. J. Akola, R. Jones, Structural phase transitions on the nanoscale: The crucial pattern in the phase-change materials $Ge_2Sb_2Te_5$ and GeTe. *Phys. Rev. B* **76**, 235201 (2007). doi:10.1103/PhysRevB.76.235201
13. J. Hegedüs, S. R. Elliott, Microscopic origin of the fast crystallization ability of Ge-Sb-Te phase-change memory materials. *Nat. Mater.* **7**, 399–405 (2008). doi:10.1038/nmat2157 Medline
14. I. Ronneberger, W. Zhang, H. Eshet, R. Mazzarello, Crystallization properties of the $Ge_2Sb_2Te_5$ phase-change compound from advanced simulations. *Adv. Funct. Mater.* **25**, 6407–6413 (2015). doi:10.1002/adfm.201500849
15. G. C. Sosso, G. Miceli, S. Caravati, F. Giberti, J. Behler, M. Bernasconi, Fast crystallization of the phase change compound GeTe by large-scale molecular dynamics Simulations. *J. Phys. Chem. Lett.* **4**, 4241–4246 (2013). doi:10.1021/jz402268v Medline
16. J. Kalikka, J. Akola, R. O. Jones, Simulation of crystallization in $Ge_2Sb_2Te_5$: A memory effect in the canonical phase-change material. *Phys. Rev. B* **90**, 184109 (2014). doi:10.1103/PhysRevB.90.184109
17. J. Kalikka, J. Akola, R. O. Jones, Crystallization processes in the phase change material $Ge_2Sb_2Te_5$: Unbiased density functional/molecular dynamics simulations. *Phys. Rev. B* **94**, 134105 (2016). doi:10.1103/PhysRevB.94.134105
18. T. H. Lee, S. R. Elliott, Ab Initio computer simulation of the early stages of crystallization: Application to $Ge_2Sb_2Te_5$ phase-change materials. *Phys. Rev. Lett.* **107**, 145702 (2011). doi:10.1103/PhysRevLett.107.145702 Medline
19. J. M. Skelton, A. R. Pallipurath, T.-H. Lee, S. R. Elliott, atomistic origin of the enhanced crystallization speed and n-type conductivity in bi-doped Ge-Sb-Te phase-change materials. *Adv. Funct. Mater.* **24**, 7291–7300 (2014). doi:10.1002/adfm.201401202
20. K. F. Kelton, G. W. Lee, A. K. Gangopadhyay, R. W. Hyers, T. J. Rathz, J. R. Rogers, M. B. Robinson, D. S. Robinson, First x-ray scattering studies on electrostatically levitated metallic liquids: Demonstrated influence of local icosahedral order on the nucleation barrier. *Phys. Rev. Lett.* **90**, 195504 (2003). doi:10.1103/PhysRevLett.90.195504 Medline
21. J. Russo, H. Tanaka, The microscopic pathway to crystallization in supercooled liquids. *Sci. Rep.* **2**, 505 (2012). doi:10.1038/srep00505 Medline
22. N. Yamada, T. Matsunaga, Structure of laser-crystallized $Ge_2Sb_{2+x}Te_5$ sputtered thin films for use in optical memory. *J. Appl. Phys.* **88**, 7020–7028 (2000). doi:10.1063/1.1314323
23. Z. Sun, J. Zhou, R. Ahuja, Structure of phase change materials for data storage. *Phys. Rev. Lett.* **96**, 055507 (2006). doi:10.1103/PhysRevLett.96.055507 Medline
24. A. V. Kolobov, P. Fons, A. I. Frenkel, A. L. Ankudinov, J. Tominaga, T. Uruga, Understanding the phase-change mechanism of rewritable optical media. *Nat. Mater.* **3**, 703–708 (2004). doi:10.1038/nmat1215 Medline
25. S. Caravati, M. Bernasconi, T. D. Kühne, M. Krack, M. Parrinello, Coexistence of tetrahedral- and octahedral-like sites in amorphous phase change materials. *Appl. Phys. Lett.* **91**, 171906 (2007). doi:10.1063/1.2801626
26. V. L. Deringer, W. Zhang, M. Lumeij, S. Maintz, M. Wuttig, R. Mazzarello, R. Dronskowski, Bonding nature of local structural motifs in amorphous GeTe. *Angew. Chem. Int. Ed.* **53**, 10817–10820 (2014). doi:10.1002/anie.201404223 Medline
27. Y. Zheng, M. Xia, Y. Cheng, F. Rao, K. Ding, W. Liu, Y. Jia, Z. Song, S. Feng, Direct observation of metastable face-centered cubic Sb_2Te_3 crystal. *Nano Res.* **9**, 3453–3462 (2016). doi:10.1007/s12274-016-1221-8
28. M. Zhu, M. Xia, F. Rao, X. Li, L. Wu, X. Ji, S. Lv, Z. Song, S. Feng, H. Sun, S. Zhang, One order of magnitude faster phase change at reduced power in Ti-Sb-Te. *Nat. Commun.* **5**, 4086 (2014). doi:10.1038/ncomms5086 Medline
29. F. Rao, Z. Song, Y. Cheng, X. Liu, M. Xia, W. Li, K. Ding, X. Feng, M. Zhu, S. Feng, Direct observation of titanium-centered octahedra in titanium-antimony-tellurium phase-change material. *Nat. Commun.* **6**, 10040 (2015). doi:10.1038/ncomms10040 Medline
30. Materials and methods are available as supplementary materials.
31. T. Siegrist, P. Jost, H. Volker, M. Woda, P. Merkelbach, C. Schlockermann, M. Wuttig, Disorder-induced localization in crystalline phase-change materials. *Nat. Mater.* **10**, 202–208 (2011). doi:10.1038/nmat2934 Medline
32. D. B. Williams, C. B. Carter, *Transmission Electron Microscopy A Textbook for Material Science* (Springer Press, New York, 2009).
33. P. Zalden, M. J. Shu, F. Chen, X. Wu, Y. Zhu, H. Wen, S. Johnston, Z. X. Shen, P. Landreman, M. Brongersma, S. W. Fong, H. S. Wong, M. J. Sher, P. Jost, M. Kaes, M. Salinga, A. von Hoegen, M. Wuttig, A. M. Lindenberg, Picosecond electric-field-induced threshold switching in phase-change materials. *Phys. Rev. Lett.* **117**, 067601 (2016). doi:10.1103/PhysRevLett.117.067601 Medline
34. B. S. Lee, G. W. Burr, R. M. Shelby, S. Raoux, C. T. Rettner, S. N. Bogle, K. Darmawikarta, S. G. Bishop, J. R. Abelson, Observation of the role of subcritical nuclei in crystallization of a glassy solid. *Science* **326**, 980–984 (2009). doi:10.1126/science.1177483 Medline
35. T. Matsunaga, J. Akola, S. Kohara, T. Honma, K. Kobayashi, E. Ikenaga, R. O. Jones, N. Yamada, M. Takata, R. Kojima, From local structure to nanosecond recrystallization dynamics in AgInSbTe phase-change materials. *Nat. Mater.* **10**, 129–134 (2011). doi:10.1038/nmat2931 Medline
36. W. Zhang, I. Ronneberger, Y. Li, R. Mazzarello, Ab initio investigation of amorphous Sb_2Te. *Chem. Month.* **145**, 97–101 (2014). doi:10.1007/s00706-013-0980-0
37. J. Kalikka, J. Akola, J. Larrucea, R. O. Jones, Nucleus-driven crystallization of amorphous $Ge_2Sb_2Te_5$: A density functional study. *Phys. Rev. B* **86**, 144113 (2012). doi:10.1103/PhysRevB.86.144113
38. K. F. Kelton, A. L. Greer, *Nucleation in Condensed Matter: Applications in Materials and Biology* (Elsevier, Oxford, 2010).

39. G. Bruns, P. Merkelbach, C. Schlockermann, M. Salinga, M. Wuttig, T. D. Happ, J. B. Philipp, M. Kund, Nanosecond switching in GeTe phase change memory cells. *Appl. Phys. Lett.* **95**, 043108 (2009). doi:10.1063/1.3191670
40. I. S. Kim, S. L. Cho, D. H. Im, E. H. Cho, D. H. Kim, G. H. Oh, D. H. Ahn, S. O. Park, S. W. Nam, J. T. Moon, C. H. Chung, High performance PRAM cell scalable to sub-20nm technology with below 4F2 cell size, extendable to DRAM applications. *Symp. VLSI Tech. Dig.* **t19b3**, 203–204 (2010).
41. A. V. Kolobov, P. Fons, J. Tominaga, Understanding phase-change memory alloys from a chemical perspective. *Sci. Rep.* **5**, 13698 (2015). doi:10.1038/srep13698 Medline
42. G. Kresse, J. Hafner, Ab initio molecular dynamics for liquid metals. *Phys. Rev. B Condens. Matter* **47**, 558–561 (1993). doi:10.1103/PhysRevB.47.558 Medline
43. J. P. Perdew, K. Burke, M. Ernzerhof, Generalized gradient approximation made simple. *Phys. Rev. Lett.* **77**, 3865–3868 (1996). doi:10.1103/PhysRevLett.77.3865 Medline
44. G. Kresse, D. Joubert, From ultrasoft pseudopotentials to the projector augmented-wave method. *Phys. Rev. B* **59**, 1758–1775 (1999). doi:10.1103/PhysRevB.59.1758
45. H. J. Monkhorst, J. D. Pack, Special points for Brillouin-zone integrations. *Phys. Rev. B* **13**, 5188–5192 (1976). doi:10.1103/PhysRevB.13.5188
46. R. Dronskowski, P. E. Blöchl, Crystal orbital Hamilton populations (COHP): Energy-resolved visualization of chemical bonding in solids based on density-functional calculations. *J. Phys. Chem.* **97**, 8617–8624 (1993). doi:10.1021/j100135a014
47. S. Maintz, V. L. Deringer, A. L. Tchougréeff, R. Dronskowski, LOBSTER: A tool to extract chemical bonding from plane-wave based DFT. *J. Comput. Chem.* **37**, 1030–1035 (2016). doi:10.1002/jcc.24300 Medline
48. V. L. Deringer, A. L. Tchougréeff, R. Dronskowski, Crystal orbital Hamilton population (COHP) analysis as projected from plane-wave basis sets. *J. Phys. Chem. A* **115**, 5461–5466 (2011). doi:10.1021/jp202489s Medline
49. A. Jain, S. P. Ong, G. Hautier, W. Chen, W. D. Richards, S. Dacek, S. Cholia, D. Gunter, D. Skinner, G. Ceder, K. A. Persson, Commentary: The Materials Project: A materials genome approach to accelerating materials innovation. *APL Mater.* **1**, 011002 (2013). doi:10.1063/1.4812323
50. T. D. Kühne, M. Krack, F. R. Mohamed, M. Parrinello, Efficient and accurate Car-Parrinello-like approach to Born-Oppenheimer molecular dynamics. *Phys. Rev. Lett.* **98**, 066401 (2007). doi:10.1103/PhysRevLett.98.066401 Medline
51. J. Hutter, M. Iannuzzi, F. Schiffmann, J. VandeVondele, cp2k: Atomistic simulations of condensed matter systems. *WIREs Comput. Mol. Sci.* **4**, 15–25 (2014). doi:10.1002/wcms.1159
52. S. Goedecker, M. Teter, J. Hutter, Separable dual-space Gaussian pseudopotentials. *Phys. Rev. B Condens. Matter* **54**, 1703–1710 (1996). doi:10.1103/PhysRevB.54.1703 Medline

ACKNOWLEDGMENTS

We acknowledge V. L. Deringer, P. Zalden, and M. Wuttig for useful discussions. F.R. gratefully thanks the support of National Natural Science Foundation of China (61622408), the Science and Technology Foundation of Shenzhen (JCYJ20170302150053136), the Strategic Priority Research Program of Chinese Academy of Sciences (XDA09020402), and the National Key Research and Development Program of China (2017YFB0701703). W.Z. gratefully thanks the support of the Youth Thousand Talents Program of China, the Young Talent Support Plan of Xi'an Jiaotong University and National Natural Science Foundation of China (61774123 and 51621063). I.R. and R.M. acknowledge the funding from Deutsche Forschungsgemeinschaft (DFG) within SFB 917 ("Nanoswitches"). E.M. is supported at JHU by U.S. DoE-BES-DMSE under grant DE-FG02-13ER46056. The authors also acknowledge the support by the International Joint Laboratory for Micro/Nano Manufacturing and Measurement Technologies, the computational resources provided by HPCC platform of Xi'an Jiaotong University, National Supercomputing Center in Shenzhen, National Supercomputer Center in Tianjin, and JARA-HPC from RWTH Aachen University under project JARA0150. Data are available in the main text and supplementary materials. A patent (application no. CN 201510697470.2) on Sc alloyed phase change materials is under examination.

SUPPLEMENTARY MATERIALS

www.sciencemag.org/cgi/content/full/science.aao3212/DC1
Materials and Methods
Figs. S1 to S11
References (*42*–*52*)

7 July 2017; accepted 30 October 2017
Published online 9 November 2017
10.1126/science.aao3212

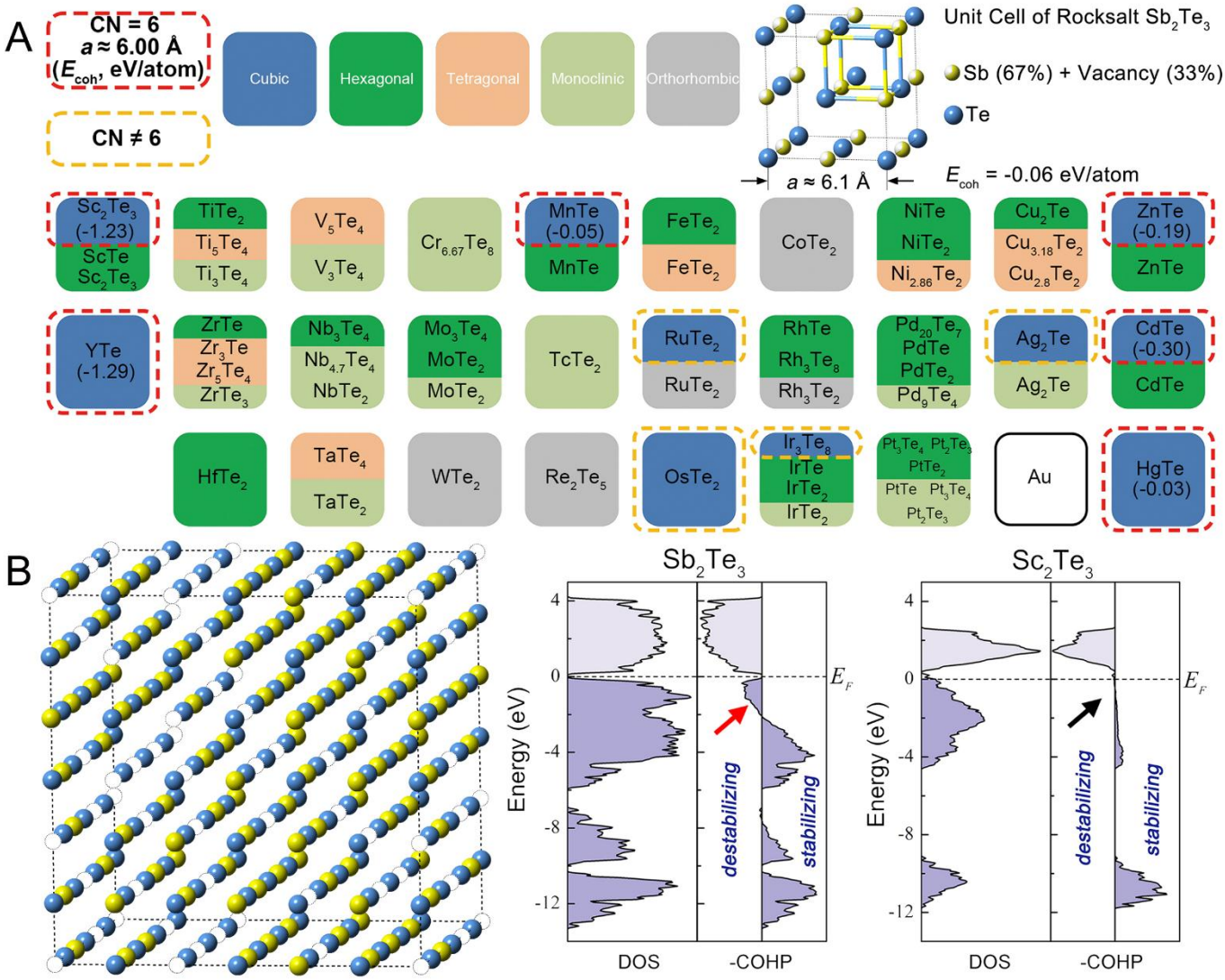

Fig. 1. Materials screening. (**A**) Screening geometrically-matched TMTs with high-strength TM-Te bonds for rocksalt Sb_2Te_3. Only TMTs compounds with T_m > 900 K are listed, in the format of the periodic table of elements. Six candidates (TM = Sc, Mn, Zn, Y, Cd, and Hg) with CN = 6 and $a \approx 6.00$ Å match closely with the rocksalt structure of Sb_2Te_3. (**B**) A 3×3×3 rocksalt Sb_2Te_3 supercell model. Atomic vacancies, Sb and Te atoms are rendered with hollow circles, yellow and blue spheres. The left and right part of the –COHP curve indicates the antibonding (destabilizing) and bonding (stabilizing) interaction, respectively.

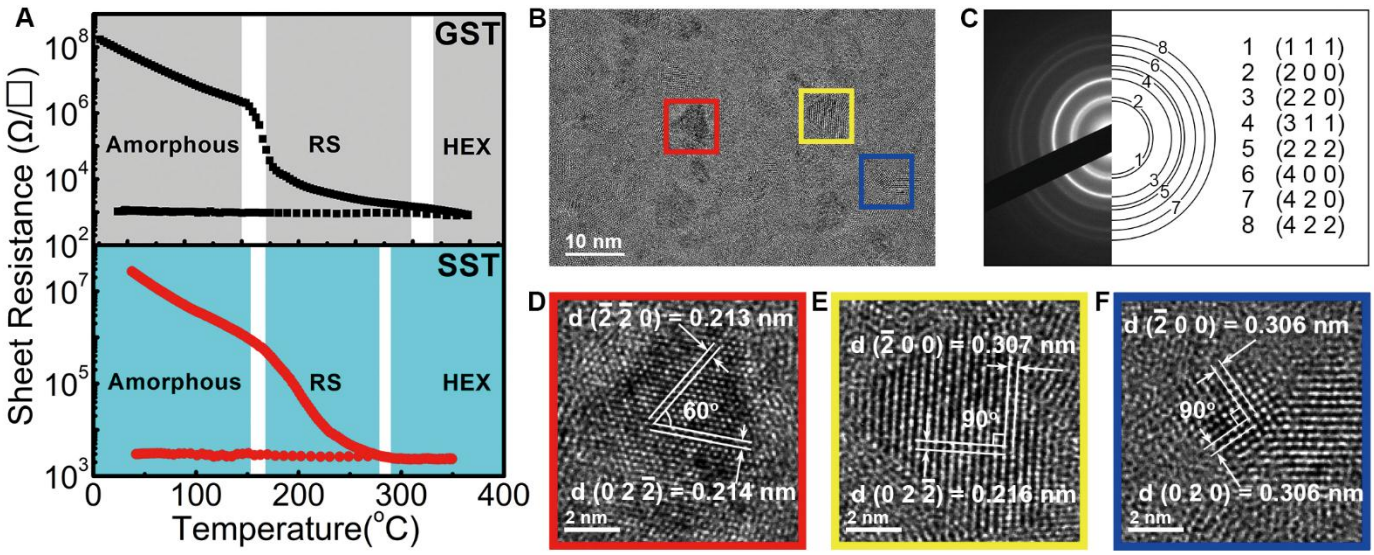

Fig. 2. Rocksalt SST. (**A**) Temperature dependence of the sheet resistance of ~300 nm-thick GST and SST films with the same heating rate of 10°C/min. Resembling GST, amorphous SST can be sequentially crystallized into metastable rocksalt (RS) and equilibrium hexagonal (HEX) phases. (**B**) TEM picture of ~20 nm-thick SST film annealed at 270°C. (**C**) The corresponding SAED pattern of (B). (**D** to **F**) High-resolution TEM images of three specific crystal grains framed in (B), project along $[1\bar{1}1]$, $[011]$, and $[001]$ zone axes, respectively.

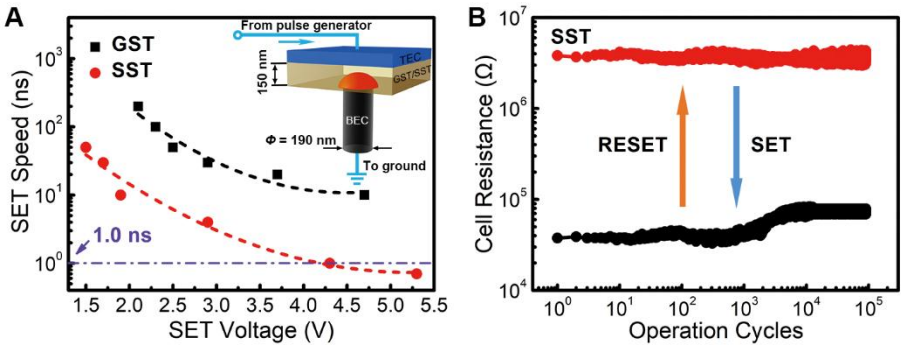

Fig. 3. PCRAM switching properties. (**A**) Voltage dependence of the SET operation speed for SST and GST PCRAM devices with the same geometry. Inset shows a schematic of the device structure with the pulse signal applied to transform the phases in the mushroom-shaped active area right above the bottom electrode contact (BEC). (**B**) Cyclability: the SST device can repeatedly perform ultrafast SET (@ 5.7 V) and RESET (@ 7.5 V) operations up to 10^5 cycles with 800 ps pulses. The RESET and SET states are stable with sustainable resistance ratio.

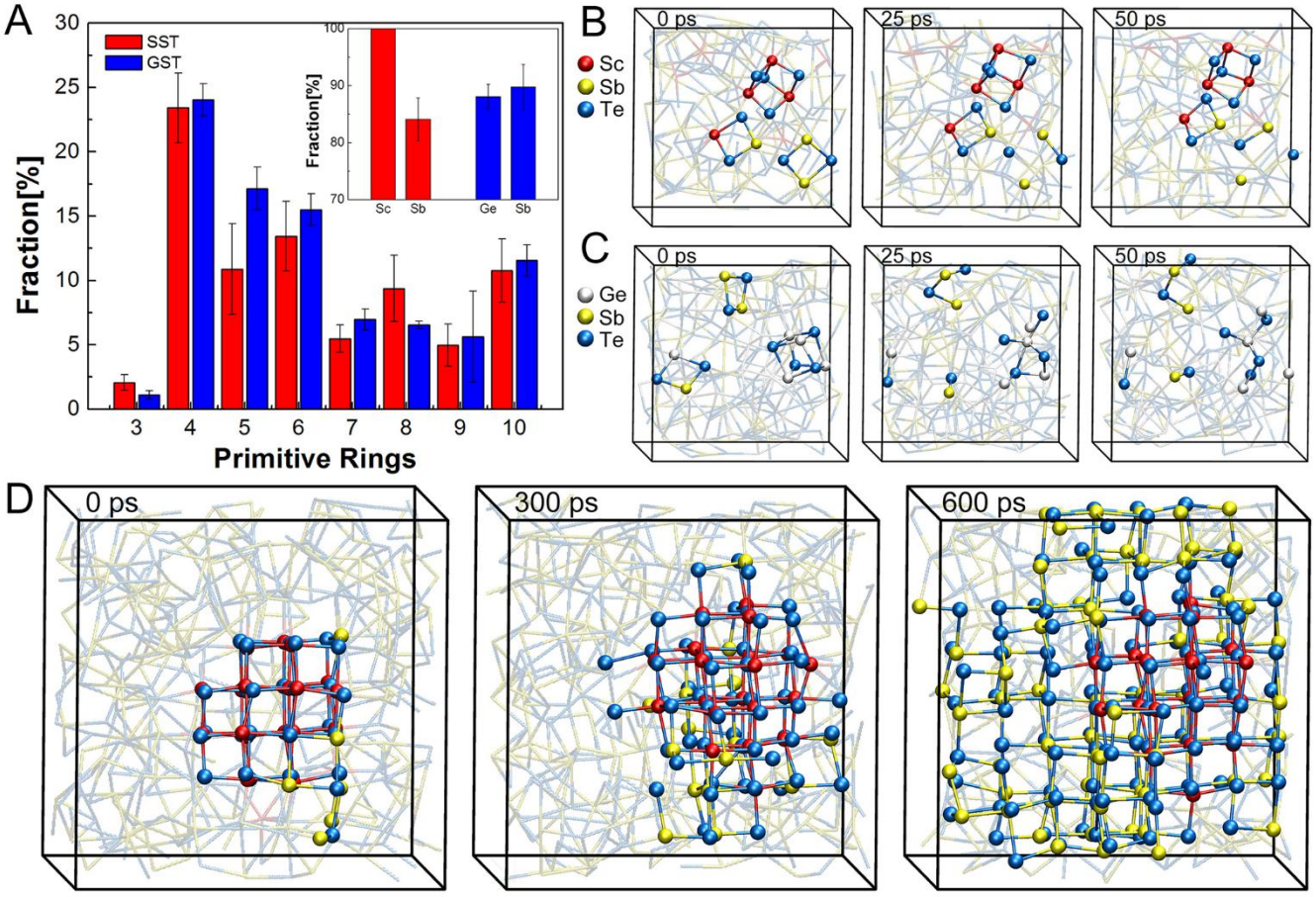

Fig. 4. DFMD simulations. (**A**) Primitive rings analysis of amorphous SST and GST. (Inset) Fraction of Sc and Sb atoms (resp. Ge and Sb atoms) involved in at least one ABAB ring. (**B** and **C**) The stability of ABAB rings in SST and GST at ~600 K. (**D**) Crystallization process of SST with a crystalline embryo in the middle at ~600 K. This seed expands steadily and quickly with time to occupy much of the box within 600 ps, in contrast to the rapid dissolution of a similar-sized seed in GST (*16*). No constraint is applied to the ScTe seed during the DFMD simulations at ~600 K. The cutoff distance for bonds is chosen as 3.4 Å, corresponding to the first valley of the pair correlation function at the same temperature, and is slightly larger than the maximum bond length (3.3 Å), determined by using sophisticated bonding analysis methods for GeTe/SbTe bonds at 0 K (*26*, *27*, *41*), to deal with thermal fluctuations at ~600 K.

Reducing the stochasticity of crystal nucleation to enable subnanosecond memory writing

Feng Rao, Keyuan Ding, Yuxing Zhou, Yonghui Zheng, Mengjiao Xia, Shilong Lv, Zhitang Song, Songlin Feng, Ider Ronneberger, Riccardo Mazzarello, Wei Zhang and Evan Ma

published online November 9, 2017